

# LUMINOSITY DEPENDENCE AND REDSHIFT EVOLUTION OF STRONG EMISSION-LINE DIAGNOSTICS IN STAR-FORMING GALAXIES<sup>1</sup>

L. L. COWIE,<sup>2</sup> A. J. BARGER,<sup>2,3,4</sup> A. SONGAILA<sup>2</sup>

*To be published in The Astrophysical Journal*

## ABSTRACT

We examine the redshift evolution of standard strong emission-line diagnostics for H $\beta$ -selected star-forming galaxies using the local SDSS sample and a new  $z = 0.2 - 2.3$  sample obtained from *HST* WFC3 grism and Keck DEIMOS and MOSFIRE data. We use the SDSS galaxies to show that there is a systematic dependence of the strong emission-line properties on Balmer-line luminosity, which we interpret as showing that both the N/O abundance and the ionization parameter increase with increasing line luminosity. Allowing for the luminosity dependence tightens the diagnostic diagrams and the metallicity calibrations. The combined SDSS and high-redshift samples show that there is no redshift evolution in the line properties once the luminosity correction is applied, i.e., all galaxies with a given  $L(\text{H}\beta)$  have similar strong emission-line distributions at all the observed redshifts. We argue that the best metal diagnostic for the high-redshift galaxies may be a luminosity-adjusted version of the [NII]6584/H $\alpha$  metallicity relation.

*Subject headings:* cosmology: observations — galaxies: distances and redshifts — galaxies: active — X-rays: galaxies — galaxies: formation — galaxies: evolution

## 1. INTRODUCTION

Over the past few years, there has been considerable interest in determining the redshift evolution of rest-frame optical emission-line ratios in star-forming galaxies. Emission-line properties can provide insight into the redshift evolution of stellar populations, gas densities, and metallicities that cannot be obtained from spectral energy distributions alone. The advent of multi-object near-infrared (NIR) spectrographs has advanced the field considerably by making it possible to obtain rest-frame optical spectra for substantial samples of high-redshift ( $z \sim 1-3$ ) galaxies, which can then be compared with local samples (e.g., Masters et al. 2014; Steidel et al. 2014; Wuyts et al. 2014; Shapley et al. 2015; Kewley et al. 2015; Yabe et al. 2015).

However, one has to be cautious with such comparisons, because high-redshift galaxies have very different properties from the general population of local galaxies. Even local galaxies with masses similar to high-redshift galaxies may be quite dissimilar in their other properties, such as their star formation rates (SFRs), morphologies, and dust content (e.g., Cowie et al. 1996).

Similar concerns apply to the use of locally-calibrated strong-line metallicity diagnostics at high redshifts. Such calibrations are based on a variety of local galaxies whose properties are generally quite different from those of high-redshift galaxies. Thus, these calibrations should not be applied uncritically at high redshifts.

It is therefore clearly important to identify appropriate lower-redshift analogs for any high-redshift galaxy comparisons. Moreover, if true analogs can be identified, then they could potentially be studied more easily. However they would have to be thoroughly tested against the properties of high-redshift galaxy samples to make sure they were representative.

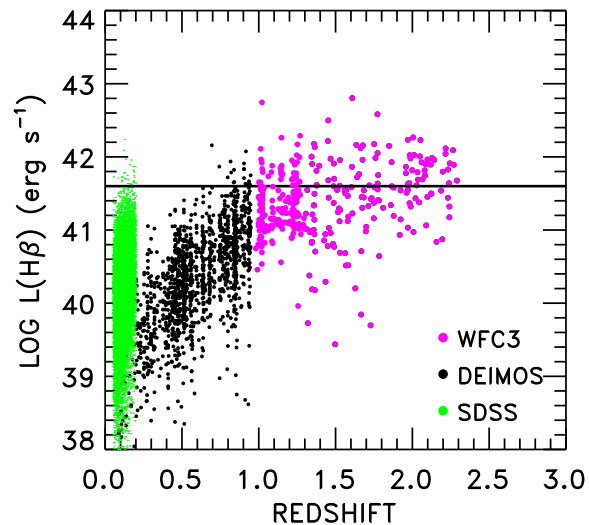


FIG. 1.— Redshift evolution of the logarithm of H $\beta$  luminosity (green symbols—every 10th data point for SDSS galaxies with  $z = 0.05 - 0.2$ ; black circles—GOODS-N galaxies from DEIMOS observations; purple circles—GOODS-N galaxies from *HST* WFC3 grism observations). We have excluded a small number of galaxies in the GOODS-N whose X-ray luminosities identify them as AGNs. The black line shows the median  $\log L(\text{H}\beta) = 41.6 \text{ erg s}^{-1}$  for the  $z > 1.35$  galaxies.

The most obvious difference between local and high-redshift galaxies is line luminosity (or, equivalently, for the Balmer lines, SFR). In Figure 1, we show the evolution of the H $\beta$  luminosity,  $L(\text{H}\beta)$ , for galaxies in the

arXiv:1512.00017v1 [astro-ph.GA] 30 Nov 2015

<sup>1</sup> Based in part on data obtained at the W. M. Keck Observatory, which is operated as a scientific partnership among the California Institute of Technology, the University of California, and NASA and was made possible by the generous financial support of the W. M. Keck Foundation.

<sup>2</sup> Institute for Astronomy, University of Hawaii, 2680 Woodlawn Drive, Honolulu, HI 96822.

<sup>3</sup> Department of Astronomy, University of Wisconsin-Madison, 475 North Charter Street, Madison, WI 53706.

<sup>4</sup> Department of Physics and Astronomy, University of Hawaii, 2505 Correa Road, Honolulu, HI 96822.

GOODS-N field (black and purple symbols) as compared with SDSS galaxies with  $z = 0.05 - 0.2$  (green symbols). (We describe both data sets in Section 2.) The most striking feature of this type of diagram is the well-known rapid rise in the line luminosity. For the  $H\beta$  line, this rise reaches a plateau beyond  $z \sim 0.8$  with a maximum luminosity of  $\log L(H\beta) \sim 42.4 \text{ erg s}^{-1}$ . A similar result has been noted for the  $\text{Ly}\alpha$  line (Wold et al. 2014).

The rapid rise and plateau results — combined with the lower luminosity bound set by the line-flux limits for  $z \gtrsim 0.8$  — give a very high luminosity selection. For the GOODS-N sample, the  $z > 1.35$  population has a median  $\log L(H\beta) = 41.6 \text{ erg s}^{-1}$  (black line). In contrast, Figure 1 shows that at low redshifts, galaxies with such a high luminosity are extremely rare.

These changes may have profound implications for the interpretation of the commonly-used strong emission-line diagnostics, especially when we are comparing low-redshift and high-redshift galaxy samples. The BPT diagram, named after Baldwin, Phillips, & Terlevich (1981) (see also Veilleux & Osterbrock 1987), plots  $\log([\text{OIII}]5007/H\beta)$  vs.  $\log([\text{NII}]6584/H\alpha)$  (hereafter,  $\text{O3H}\beta$  versus  $\text{N2H}\alpha$ ). Originally developed to determine the ionizing mechanism in emission-line galaxies (i.e., star formation vs. active galactic nucleus activity), it has recently been used to compare the excitation properties of high-redshift star-forming galaxies with those of local star-forming galaxies. Unfortunately, however, such comparisons are complicated by the fact that the BPT diagram is biased: galaxies with a higher SFR (or, equivalently, Balmer line luminosity) lie above the average BPT locus at a given mass (Brinchmann et al. 2008; Salim et al. 2014; Newman et al. 2014; Salim et al. 2015).

Juneau et al. (2014) emphasized the importance of this effect in interpreting the line properties of high-redshift galaxies. They postulated that much of the apparent redshift evolution of the line properties could in fact be a luminosity selection effect, in which only the high-SFR portion of the BPT star-forming galaxy locus at high redshifts (which is the only portion being sampled) is being compared with the median of the BPT star-forming galaxy locus locally. However, they stressed that the rarity of the high line-luminosity galaxies at low redshift means that they could be substantially different from the high-redshift galaxies of the same luminosity, making it hard to differentiate between selection bias and evolution.

However, as we shall show in the present paper, all of the line ratios have a strong and well-defined dependence on the Balmer-line luminosity, suggesting that the low-redshift high-luminosity galaxies may in fact be close analogs of the high-redshift galaxies. Correcting for this luminosity dependence considerably tightens all of the various diagnostic diagrams, and including  $L(H\beta)$  as an additional parameter improves the metallicity estimators. This correction also removes any redshift evolution in the line ratios since the higher-redshift objects closely match lower-redshift samples in the same Balmer-line luminosity range.

Throughout, we use the observed  $L(H\beta)$ , without an extinction correction, as our variable, which allows for simple corrections to any data set. We use  $L(H\beta)$  rather than  $L(H\alpha)$ , which is contaminated by  $[\text{NII}]$  in low-

resolution spectra. However, since the extinction correction smoothly varies with luminosity, we would expect to see the same type of line-ratio dependence on the extinction-corrected values or SFRs. In the low-redshift SDSS data described in Section 2.1, the mean extinction corrections are almost independent of Balmer-line luminosity, and the results of the present paper can be converted to  $L(H\alpha)$  using the relation  $\log L(H\alpha) = \log L(H\beta) + 0.54$ . The SFR for a Kroupa (2001) IMF is given by a mean relation of  $\log \text{SFR} = \log L(H\beta) - 40.50$ , where the SFR is in  $M_{\odot} \text{ yr}^{-1}$  and  $L(H\beta)$  is in  $\text{erg s}^{-1}$  based on the SFRs of Brinchmann et al. (2004), as updated in the current data release. (For a modified Salpeter IMF (Kennicutt 1998), the SFR would be a factor of 1.5 higher.) The intermediate-redshift data also show an extinction that is independent of line luminosity and gives a broadly similar correction to  $\log L(H\alpha) = \log L(H\beta) + 0.58$ . The situation at the highest redshifts ( $z \sim 2$ ) is less clear, and there may be a dependence on line luminosity (Reddy et al. 2015), though this effect may be, at least partly, selection bias. However, the average conversion from  $H\beta$  to  $H\alpha$  is similar, with  $\log L(H\alpha) = \log L(H\beta) + 0.54$  for the galaxies with detected  $H\beta$ . Some of the possible complexities in interpreting the line luminosities are described in Stasińska et al. (2015).

In Section 2, we present the SDSS data that we use and our highly complete optical and NIR spectroscopic sample of galaxies with  $z = 0 - 2.3$  in the GOODS-N field. In Section 3, we focus on the BPT diagram from the SDSS data and show that there is a simple dependence of the star-forming galaxy locus on Balmer-line luminosity. In Section 4, we show that the positions of high-redshift galaxies in the BPT and other diagnostic diagrams are similar to those of SDSS galaxies with comparable luminosities. This suggests that we can use these latter objects as surrogates for the high-redshift population. In Section 5, we use the properties of the high-luminosity SDSS galaxies to determine what is causing the changes in the diagnostic diagrams with luminosity. We summarize our results in Section 6.

## 2. DATA SETS

### 2.1. SDSS ( $z=0.05-0.2$ )

Our local sample is taken from the Sloan Digital Sky Survey Data Release 7 (SDSS DR7; Abazajian et al. 2009), restricted to  $z > 0.05$  to minimize aperture effects. We use the line fluxes from the Value Added Catalogs of the Max-Planck Institute for Astronomy (Garching) and John Hopkins University (MPA/JHU)<sup>5</sup>. Tremonti et al. (2004) and Brinchmann et al. (2004) give details on the methods that were used to develop this catalog. Even in this redshift range we need to correct the fluxes in the fibers to total fluxes in order to compare properly with high-redshift samples. We follow the standard procedure of multiplying the observed flux in the fiber by the ratio of the total continuum flux to the continuum flux in the fiber. This is clearly approximate since it assumes that the line emission has the same spatial distribution as the continuum, but represents our best estimate of the correction. The correction is near unity for the galaxies with the highest line luminosities though it can be significantly

<sup>5</sup> <http://www.mpa-garching.mpg.de/SDSS/DR7/>

larger in the low-luminosity objects, rising to an average correction of approximately a factor of seven for a fiber  $\log L(\text{H}\beta)$  in  $\text{erg s}^{-1}$  of 39. Because the correction for the high-luminosity objects is small, the comparison with the high-redshift high-luminosity objects is not significantly affected by including this effect. These spectra have been corrected for underlying stellar absorption. We restrict consideration to sources with  $\text{S/N} > 10$  in  $\text{H}\beta$  line flux and compute line luminosities and the various diagnostic line ratios, including  $\text{O3H}\beta$  and  $\text{N2Ha}$ , for this sample. We also consider only galaxies with  $z = 0.05 - 0.2$ . We hereafter refer to this as the “full” SDSS sample.

### 2.2. DEIMOS ( $z=0.2-0.95$ )

We made DEIMOS observations in a number of runs between 2004 and 2015 with the goal of obtaining consistently high-quality optical spectra of all of the 2850  $B < 25$  galaxies in the uniformly-covered portion of the *HST* GOODS-N field. We have now observed all but six of these galaxies, and we have obtained robust redshifts for 2501 (88%), many of which are published in Cowie et al. (2004) and Barger et al. (2008). We used the  $600 \text{ l mm}^{-1}$  grating, giving a resolution of  $3.5 \text{ \AA}$  and a wavelength coverage of  $5300 \text{ \AA}$ , which was also the configuration used in the KTRS observations (Wirth et al. 2004). We have incorporated archival data, particularly from KTRS, but many of these spectra have relatively poor sky subtraction, and we re-observed them, whenever necessary, to obtain higher-quality spectra. We centered the spectra at an average wavelength of  $7200 \text{ \AA}$ , though the exact wavelength range for each spectrum depends on the slit position. We broke each  $\sim 1 \text{ hr}$  exposure into three sub-exposures, stepping the galaxies along the slit by  $1''.5$  in each direction. We continuously re-observed unidentified galaxies or galaxies with poor spectra, giving maximum exposure times of up to 7 hrs. The spectra were reduced following the procedures described in Cowie et al. (1996). Our dithering procedure provides extremely high-precision sky subtraction, which is important for measuring accurate equivalent widths.

We measured the line widths, redshifts, amplitudes, and continuum level for the suite of observable lines in the one-dimensional spectra using the MPFIT program of Markwardt (2009). For the weaker lines, we measured only the amplitudes, and adopted the line-widths and redshifts from the strongest neighboring line (where available,  $[\text{OIII}]5007$ ,  $\text{H}\alpha$ , and  $[\text{OII}]3727$ ; for the latter, we measured both members of the doublet separately).

Because of the difficulties in making a precise spectrophotometric calibration of the multi-slit DEIMOS data, we used an indirect method to calculate the fluxes. We matched the contributions of the lines plus continuum to the observed *HST* magnitude for the corresponding broadband filter. We then determined errors for each line by fitting random positions in the spectra in the neighborhood of the line. Finally, we accounted for underlying absorption using fixed corrections of  $3 \text{ \AA}$  and  $2 \text{ \AA}$  for the equivalent widths of the  $\text{H}\beta$  and  $\text{H}\alpha$  lines, respectively. These match the average corrections in the SDSS data.

We found 83 galaxies with  $\text{H}\beta$  detected at  $> 10\sigma$  between  $z = 0.2 - 0.5$ , where we can measure both  $\text{O3H}\beta$  and  $\text{N2Ha}$  from the DEIMOS spectra. These provide a

nearly complete sample above  $\log L(\text{H}\beta)=40.0 \text{ erg s}^{-1}$  (see Figure 1). We found 180 galaxies with  $\text{H}\beta$  detected at  $> 10\sigma$  between  $z = 0.5 - 0.95$ , where only  $\text{O3H}\beta$  can be measured from the DEIMOS spectra. Here the completeness limit is  $\log L(\text{H}\beta)=40.5 \text{ erg s}^{-1}$ . To get  $\text{N2Ha}$  determinations for these galaxies requires MOS-FIRE spectra in the  $Y$  and  $J$  bands (see §2.4).

### 2.3. HST Grism ( $z \geq 0.95$ )

For galaxies at  $z \geq 0.95$ , we measured the Balmer-line luminosities from the *HST* WFC3 G141 and G102 grism observations covering nearly all of the GOODS-N field (PIs B. Weiner and G. Barro, respectively). While these data have now been incorporated into the 3D-HST sample (Brammer et al. 2012), we used our own extractions that we made from the raw data using the aXe software package supported by STScI. We extracted spectra for 5709 galaxies with AB magnitudes brighter than 24.5 in the F140W band. We formed one-dimensional spectra over the full galaxy areas, as defined by the corresponding continuum image. We show a typical spectrum in Figure 2.

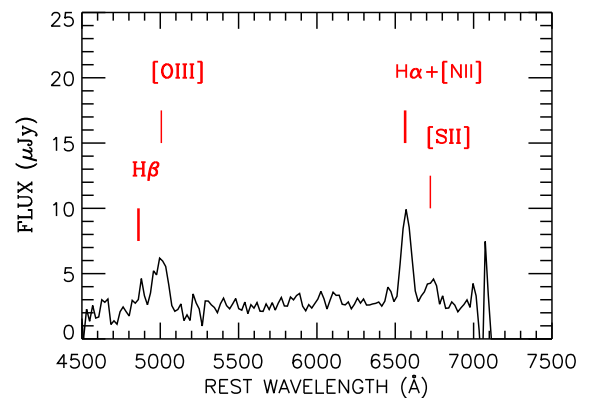


FIG. 2.— WFC3 G141 grism spectrum of a  $z = 1.39$  galaxy with  $\log L(\text{H}\alpha+[\text{NII}])=42.16 \text{ erg s}^{-1}$ . The  $\text{H}\alpha + [\text{NII}]6548,6584$  blend is marked, as are the  $[\text{OIII}]4959,5007 + \text{H}\beta$  complex and the  $[\text{SII}]6717,6734$  blend.

We can make precise line-flux measurements with the grism data, since, in contrast with the ground-based data, there are no issues of slit losses or photometric conditions. However, the resolution is low:  $R \sim 130$  in the G141 grism over the wavelength range  $1.1 - 1.7 \mu\text{m}$  and  $R \sim 210$  in the G102 grism over the wavelength range  $0.8 - 1.15 \mu\text{m}$ , with the exact value depending on the size and shape of the galaxy. This means that the  $\text{H}\alpha$  line is blended with the  $[\text{NII}]6548,6584$  lines, and the  $[\text{OII}]3727$  and  $[\text{SII}]6717,6734$  doublets are unresolved (see Figure 2). However, the lines in the  $[\text{OIII}]4959,5007$  and  $\text{H}\beta$  complex can be fitted to determine the  $\text{H}\beta$  fluxes. We did this in the following way: We measured the  $[\text{OIII}]5007$  and  $\text{H}\beta$  fluxes from the one-dimensional spectra using MPFIT. We then forced the  $[\text{OIII}]4959$  line to a value of 0.326 times the  $[\text{OIII}]5007$  line and fitted all three lines in the complex simultaneously using a single redshift and line-width. For  $\text{H}\alpha$ , we measured the combined  $\text{H}\alpha+[\text{NII}]$  line flux. Once again, we corrected for underlying absorption using fixed corrections of  $3 \text{ \AA}$  and

2 Å for the equivalent widths of the H $\beta$  and H $\alpha$  lines.

We are interested in using the grism data primarily to find galaxies in the redshift ranges  $z = 1.38 - 1.74$  and  $z = 2.03 - 2.65$ , where O3Hb and N2Ha can be simultaneously measured from ground-based MOSFIRE data (Section 2.4). For redshifts  $z \gtrsim 1.52$ , the H $\alpha$  line is no longer observable in the grism data, and we rely on H $\beta$ , which is observable in the G141 grism data through the whole lower redshift interval and out to  $z = 2.30$  in the upper interval.

Over  $z = 1.30 - 1.52$ , both the H $\alpha$  and H $\beta$  lines are in the grism data, so we determine the completeness of the H $\beta$  selection by seeing at what point we start to miss H $\alpha$  sources in H $\beta$ . Based on this analysis, we adopt a flux selection of  $f(\text{H}\beta) = 5 \times 10^{-18} \text{ erg cm}^{-2} \text{ s}^{-1}$ , which corresponds to a luminosity limit of  $\log L(\text{H}\beta) = 41 \text{ erg s}^{-1}$  for  $z = 1.38 - 1.74$  and  $\log L(\text{H}\beta) = 41.5 \text{ erg s}^{-1}$  for  $z = 2.03 - 2.30$ . These selections give samples of 43 and 28 galaxies, respectively.

#### 2.4. MOSFIRE

In order to measure the standard diagnostic line ratios, we need higher-resolution data than the *HST* grism spectra can provide. We therefore made follow-up observations of the luminosity-selected sample using the MOSFIRE NIR spectrograph on the Keck I telescope (McLean et al. 2012). The ground-based NIR windows (and the corresponding MOSFIRE filters) limit the redshift intervals in which the line ratios can be measured. We illustrate this in Figure 3, where for each of the N2Ha and O3Hb ratios, we show the redshift interval where the ratio can be measured (black for optical from DEIMOS, gold for *Y*-band, blue for *J*-band, green for *H*-band, and purple for *K*-band). The gray shading shows where it is possible to measure both ratios via some combination of instruments and bandpasses; this encompasses nearly the full  $z = 0 - 1$  interval, as well as the intervals  $z = 1.38 - 1.74$  and  $z = 2.03 - 2.65$ .

We obtained MOSFIRE observations of the H $\beta$  luminosity-selected galaxies during three two-night runs from 2013 to 2015. We focused on galaxies with redshifts that allowed measurement of all of the line diagnostics. However, MOSFIRE can configure up to 46 slits and, since the target sources were too sparse to fill the masks, we also observed high-luminosity galaxies outside these redshifts, together with filler targets. We used a 0".7 slit width and made observations in the *J* (24 min exposure), *H* (16 min), and *K* (24 min) bands with an ABBA stepping pattern, where the A position is 1.25" below the nominal position, and the B position is 1.25" above the nominal position. We carried galaxies into subsequent masks when additional exposure time was required. In addition, we searched the KOA archive for all publicly-available data (obtained prior to May 2014) on the GOODS-N. In total, our own observations plus the archival data provided spectra for 404 galaxies, of which 177 have identifiable NIR emission lines that make it possible to measure redshifts. We show the galaxies with measured MOSFIRE redshifts in Figure 3 (red squares).

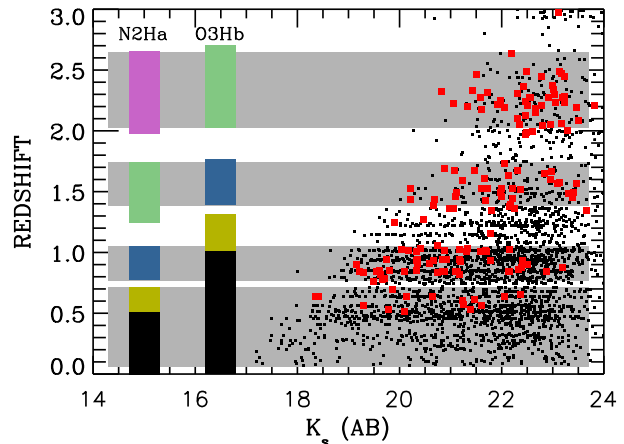


FIG. 3.— Redshift vs.  $K_s$  magnitude for the GOODS-N (black squares). Galaxies with MOSFIRE spectra from which the redshift can be measured are shown with larger red squares. The redshifts at which the N2Ha and O3Hb ratios (colored bars) can be measured are shown on the left. The colors mark the MOSFIRE filter in which the lines lie (gold—*Y*, blue—*J*, green—*H*, and purple—*K*), while black marks where the lines are covered by the DEIMOS spectra. The gray shading shows the redshift ranges in which some combination of instruments and bandpasses allows both ratios to be measured. (We ignore the tiny region around  $z \sim 1.2 - 1.3$  where the green and gold bars overlap.)

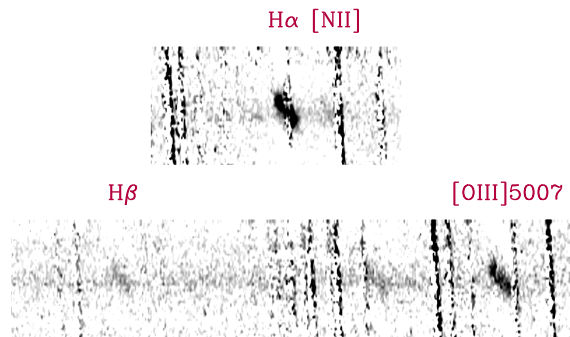


FIG. 4.— Spectral images around the H $\alpha$  + [NII] complex (upper spectrum) and around the H $\beta$  + [OIII] complex (lower spectrum) for a galaxy at  $z = 1.432$  with  $\log L(\text{H}\beta) = 42.5 \text{ erg s}^{-1}$ . Note the shape of the lines in the wavelength (*x*-axis) vs. spatial position on the slit (*y*-axis), and also the contamination of portions of the spectral features by strong night sky lines.

We extracted the spectra using our own IDL-based package. Each exposure was flat-fielded using dome flats taken in the afternoon, and cosmic rays and bad pixels were flagged out. We then adjusted the normalization of each exposure in the ABBA pattern to provide an optimal matching of the strength of the night sky lines in each of the four exposures. Both the A exposures and the B exposures were summed. We then subtracted the summed B image from the summed A image to form a differenced image, which removes the sky lines. We shifted the differenced image by 2".5 so that the positive A in the shifted differenced image lay at the position of the negative B in the unshifted differenced image. We then subtracted the unshifted differenced image from the

shifted differenced image to form the final ABBA image, which contains the positive spectrum together with two negative residuals on either side (Figure 4).

We also formed the corresponding two-dimensional sky image by summing the ABBA frames shifted in the same way. We made fits to the sky lines together with calibration spectra taken in the the afternoon to form the wavelength calibration as a function of spatial position in the two-dimensional image, and then we combined the multiple exposures in each bandpass. Because of the extreme stability of MOSFIRE, we did not find it necessary to further register these images in either the spatial or wavelength axes. We show sections of a typical two-dimensional image in Figure 4.

In contrast to the DEIMOS spectra, the continua in the MOSFIRE spectra are often too weak to measure equivalent widths, so we measured flux ratios directly. Since the flux ratios are only of neighboring lines, we do not need accurate spectrophotometry. To account for underlying absorption, we measured equivalent widths in the grism data and applied fixed corrections of 3 Å and 2 Å for H $\beta$  and H $\alpha$ , respectively. Where H $\alpha$  was not covered by the grism data, we computed the H $\alpha$  equivalent width from H $\beta$  using the median value of the EW(H $\alpha$ )/EW(H $\beta$ ) ratio determined from the sources where both were measured. Most of the galaxies have corrections which are close to the median values of 0.89 in [OIII]/H $\beta$  and 0.98 in [NII]/H $\alpha$ . Thus the use of a single correction value for each line ratio as in Steidel et al. (2014) (who used 0.85 for [OIII]/H $\beta$  and 1 for [NII]/H $\alpha$ ) provides a good approximation. Removing the absorption correction would raise O3Hb by 0.07 in the high-redshift galaxies.

We also work with the two-dimensional spectral images rather than extracting one-dimensional spectra. There are two reasons for following this course, which we illustrate in Figure 4. The first is that the two-dimensional spectral images often show resolved velocity structure. In these cases, extracting a one-dimensional spectrum adds unnecessary noise relative to working directly with the two-dimensional spectral image. The second is the strength of the night-sky lines in the NIR, which can greatly increase the noise. In the upper panel of Figure 4, we see that portions of the H $\alpha$  and [NII]6584 lines are severely contaminated in this way. By extracting the fluxes from the two-dimensional spectral images, we can avoid these regions.

For both N2Ha and O3Hb, we are measuring a weaker line ([NII]6584 or H $\beta$ ) relative to a stronger neighboring line (H $\alpha$  or [OIII]5007). We made an optimal extraction from the two-dimensional spectral image by forming an integral of the two-dimensional spectral image of the weaker line weighted by the two-dimensional intensity of the stronger line, excluding any regions covered in either by the strongest night-sky lines, and dividing by the integral of the two-dimensional spectral image of the stronger line with the same weighting. Once again, we determined the noise levels by randomizing the wavelength positions of the weaker line and measuring the ratio at these positions.

### 3. LOCAL RELATIONS FROM THE SDSS DATA

We start by re-examining the dependence of the BPT star-forming galaxy locus (the left wing of the BPT diagram) on Balmer-line luminosity and redshift using the

SDSS sample. In Figure 5(a), we show the BPT diagram for the full SDSS sample in intervals of  $\log L(\text{H}\beta)$  ranging from 39 – 39.5  $\text{erg s}^{-1}$  (black squares) to 41 – 42  $\text{erg s}^{-1}$  (purple squares). For each  $\log L(\text{H}\beta)$  interval, we show the median values of O3Hb in 0.2 dex bins of N2Ha. The sizes of the squares represent the number of sources in each bin.

We immediately see the known result that at higher  $L(\text{H}\beta)$  luminosities, O3Hb is high at a given N2Ha and N2Ha is high at a given O3Hb (Brinchmann et al. 2008; Juneau et al. 2014; Salim et al. 2014). More profoundly, however, we see that the shape of the star-forming galaxy locus remains roughly invariant with  $\log L(\text{H}\beta)$ . It is only the normalization of O3Hb relative to N2Ha that is changing as a function of  $\log L(\text{H}\beta)$ .

Motivated by Figure 5(a), we fitted the dependence of O3Hb on N2Ha and  $L(\text{H}\beta)$  for the star-forming galaxy locus (N2Ha < -0.5) using the MPFIT2DFUN two-dimensional fitting routine from Markwardt (2009). We adopted a third-order fit for the dependence on N2Ha and a linear fit for the dependence on  $\log L(\text{H}\beta)$ . Including the luminosity dependence by shifting N2Ha, we find

$$x = \text{N2Ha} - 0.09(\log L(\text{H}\beta) - 40.5), \quad (1)$$

and

$$\text{O3Hb} = -1.85 - 4.02x - 2.18x^2 - 0.42x^3. \quad (2)$$

Alternatively, we can include the luminosity dependence by shifting O3Hb, giving

$$\text{O3Hb} = -1.85 - 4.02(\text{N2Ha}) - 2.18(\text{N2Ha})^2 - 0.42(\text{N2Ha})^3 + 0.09(\log L(\text{H}\beta) - 40.5). \quad (3)$$

In Figures 5(b) and (c), we show the effects of applying the above luminosity offsets in N2Ha and O3Hb, respectively, to the SDSS data to normalize to  $\log L(\text{H}\beta) = 40.5 \text{ erg s}^{-1}$ . Either offset aligns the star-forming galaxy loci across the luminosity range and, based solely on the BPT diagram, variation in either variable or a combination of both could produce the measured offsets.

We find that the formal errors on the coefficients are extremely small. However, when we vary the fitting ranges for both redshift and N2Ha, and when we adjust the  $L(\text{H}\beta)$  S/N away from the adopted value of 10 (see Section 2.1), we find larger systematic errors. In particular, the  $\log L(\text{H}\beta)$  coefficient in both sets of equations can range from 0.08 to 0.10, depending on these choices.

The luminosity offset is not simply a shift in the medians, as we illustrate in Figure 6, where we plot the BPT diagram for the individual SDSS points in  $\log L(\text{H}\beta)$  intervals of (a) 41.25 – 41.75 and (b) 40.25 – 40.75  $\text{erg s}^{-1}$ , each separated into two redshift intervals (black for  $z = 0.1 - 0.2$  and red for  $z = 0.05 - 0.1$ ).



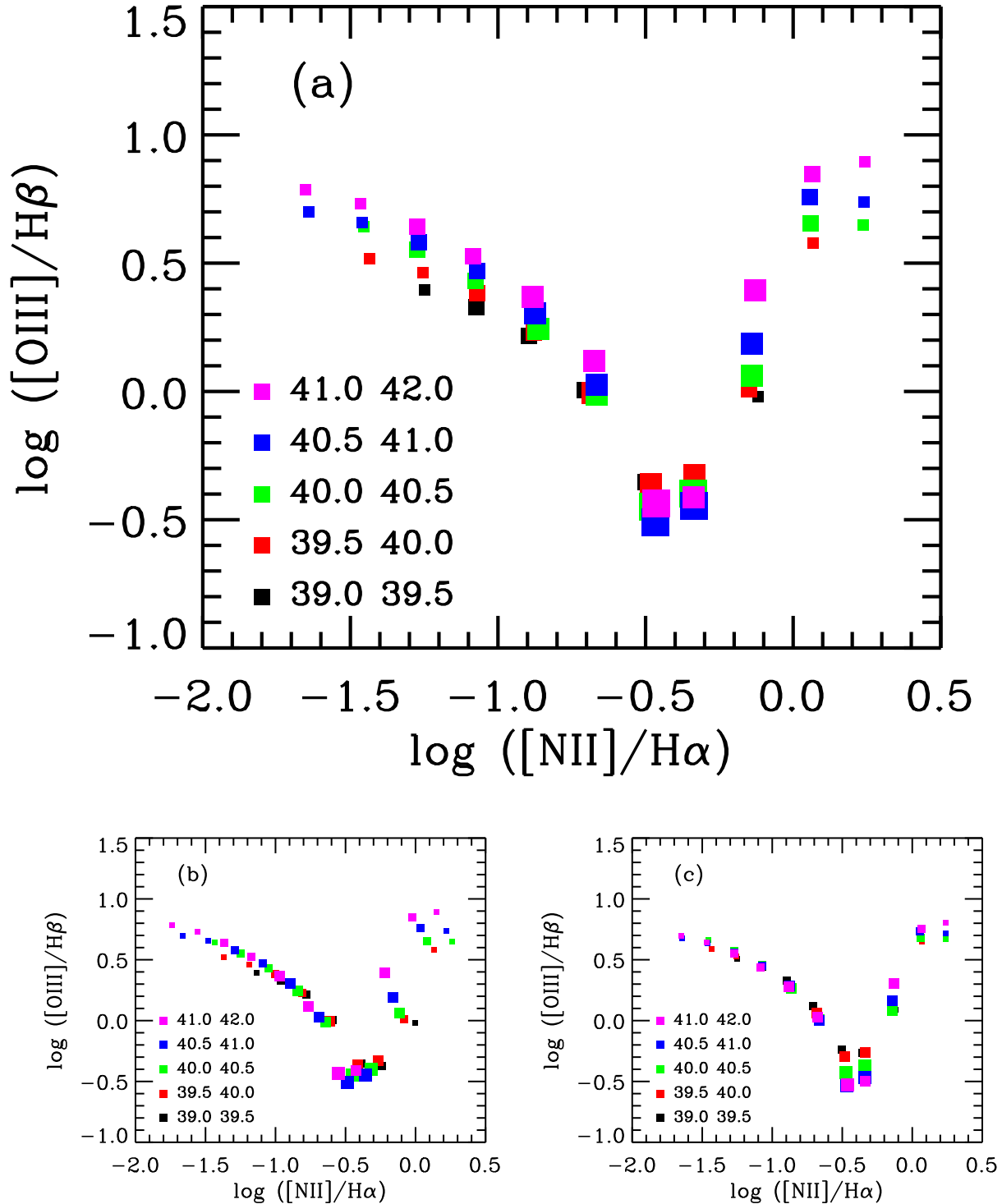


FIG. 5.— (a) BPT diagram for the full SDSS sample in intervals of  $\log L(\text{H}\beta)$  (colors). We show the median values of O3Hb in 0.2 dex bins of N2Ha (squares). The sizes of the squares represent the number of sources in each bin, ranging from 10–100 (smallest), 100–1000, 1000–10000, to 10000–100000 (largest). In the star-forming galaxy locus (the left wing of the BPT diagram; N2Ha < -0.5), the normalization of O3Hb relative to N2Ha rises with  $L(\text{H}\beta)$ . In (b) and (c), respectively, we show the effects of introducing an offset in N2Ha using Equations 1 and 2 and in O3Hb using Equation 3 to normalize to  $\log L(\text{H}\beta) = 40.5 \text{ erg s}^{-1}$ . Either offset approximately aligns the BPT star-forming galaxy locus.

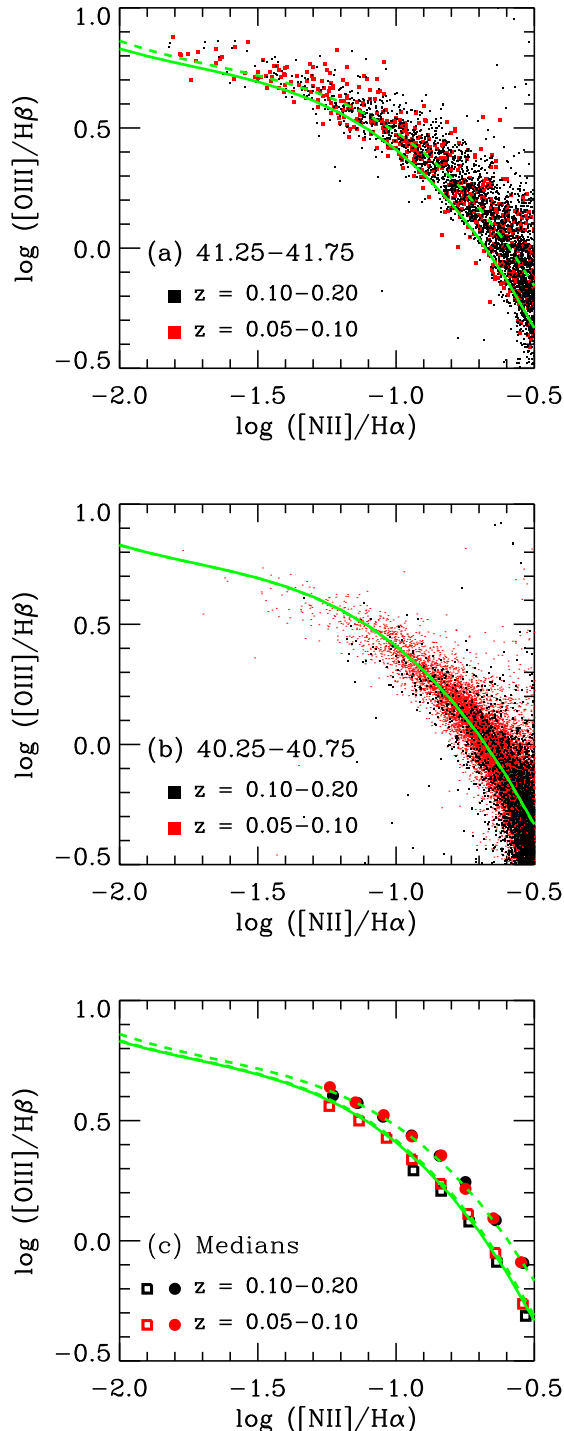


FIG. 6.— BPT diagrams for the full SDSS sample in two luminosity intervals of  $\log L(\text{H}\beta)$ , (a) 41.25 – 41.75 and (b) 40.25 – 40.75  $\text{erg s}^{-1}$ , each separated into two redshift intervals (red squares— $z = 0.05 - 0.1$ ; black squares— $z = 0.1 - 0.2$ ). The green solid curve in both panels shows the fit to the star-forming galaxy locus of the full SDSS sample at the median  $\log L(\text{H}\beta) = 40.5 \text{ erg s}^{-1}$ , while the green dashed curve in panel (a) shows the luminosity-offset locus using Equations 1 and 2, which vary N2Ha, evaluated at  $\log L(\text{H}\beta)$  of 41.5. Panel (c) shows the median values of N2Ha for the two samples with the circles showing the high luminosity interval of panel (a) and the open squares the lower luminosity interval of panel (b).

There is essentially no difference between the source distributions for the two redshift intervals in either panel. There is, however, an increase in N2Ha relative to O3Hb for the higher-luminosity points in (a). This can clearly be seen by plotting the fit to the star-forming galaxy locus of the full SDSS sample at the median  $\log L(\text{H}\beta) = 40.5 \text{ erg s}^{-1}$  (green solid curve), along with the luminosity-offset loci (green dashed curve) determined by evaluating Equations 1 and 2, which vary N2Ha, at  $\log L(\text{H}\beta)$  of (a) 41.5  $\text{erg s}^{-1}$  and (b) 40.5  $\text{erg s}^{-1}$ . As expected, the higher-luminosity points in (a) lie uniformly above the green solid curve but generally along the green dashed curve, while the lower-luminosity points in (b) are consistent with the green solid curve, which is nearly identical to the green dashed curve. The agreement may be more clearly seen in panel (c) where we show the medians in each luminosity and redshift interval compared with the fits.

#### 4. COMPARISON WITH HIGHER-REDSHIFT SAMPLES

Having established the dependence of the BPT star-forming galaxy locus on Balmer-line luminosity (but not redshift) for the SDSS local sample, we turn our attention to the higher-redshift samples. As we did in Figure 6, we start in Figure 7 by plotting the SDSS data in two well-separated  $\log L(\text{H}\beta)$  intervals, this time using 39.0 – 40.0  $\text{erg s}^{-1}$  (black dots) and 41.5 – 42.5  $\text{erg s}^{-1}$  (light green squares). The green curve is again the fit to the star-forming galaxy locus of the full SDSS sample at the median  $\log L(\text{H}\beta) = 40.5 \text{ erg s}^{-1}$ . Compared to this curve, the lower-luminosity points lie uniformly low, while the higher-luminosity points lie uniformly high.

Next, we plot our high-redshift galaxies, including every source with a well-measured ( $> 3\sigma$ ) O3Hb (purple circles). To increase the sample size, we also plot the high-redshift galaxies from Steidel et al. (2014, orange squares) and Shapley et al. (2015, orange circles). We show galaxies with only upper limits on N2Ha at their  $2\sigma$  limits (leftward pointing arrows).

All three high-redshift galaxy samples overlap substantially with one another and are broadly consistent, though our luminosity-selected sample extends to somewhat lower values of N2Ha, while the mass-selected sample of Shapley et al. (2015) is slightly higher in N2Ha. The Steidel et al. (2014) sample lies in between. Note that some of the sources are likely AGNs, given their locations on the diagram.

The most striking observation from Figure 7 is how similar the high-redshift data are to the higher-luminosity SDSS data for the star-forming galaxy locus. This emphasizes how critical it is to choose appropriate counterparts when comparing high-redshift samples with low-redshift ones.

The similarity of the high-redshift data to the higher-luminosity SDSS data is not unique to the BPT diagram. In Figure 8, we show two alternative diagnostic diagrams that are frequently used, (a)  $[\text{NII}]6584/[\text{OII}]3726,3729$  (N2O2) versus O3Hb and (b)  $[\text{NII}]6584/[\text{SII}]6717,6731$  (N2S2) versus O3Hb. In both cases, the denominator is the sum of the fluxes from both members of the doublet. For N2O2, we include an extinction correction because of the wide wavelength separation of the lines. We plot

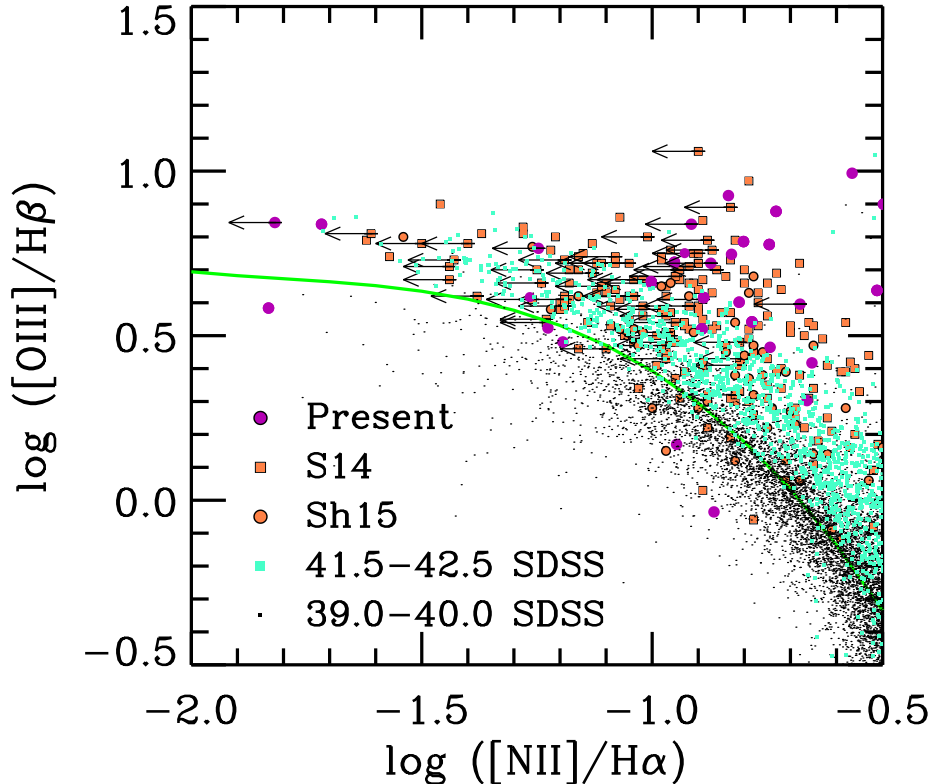


FIG. 7.— BPT diagram for the full SDSS sample in two intervals of  $\log L(\text{H}\beta)$  (black dots— $39.0 - 40.0 \text{ erg s}^{-1}$ ; light green squares— $41.5 - 42.5 \text{ erg s}^{-1}$ ). The green solid curve shows the fit to the star-forming galaxy locus ( $\text{N2Ha} < -0.5$ ) of the full SDSS sample at the median  $\log L(\text{H}\beta) = 40.5 \text{ erg s}^{-1}$ . For comparison, we show our data (every source with  $\text{O3Hb} > 3\sigma$ ; purple circles), along with the high-redshift data from Steidel et al. (2014, orange squares) and Shapley et al. (2015, orange circles). Sources with only upper limits on  $\text{N2Ha}$  are plotted at the  $2\sigma$  values with leftward pointing arrows. Some of the sources are likely AGNs, given their locations on the diagram. For the star-forming galaxy locus, the positions in the diagram of the high-redshift galaxies closely match those of the higher-luminosity SDSS galaxies.

the SDSS data in the same two well-separated  $\log L(\text{H}\beta)$  intervals as in Figure 7.

We fitted the dependence of  $\text{N2S2}$  on  $\text{O3Hb}$  and  $L(\text{H}\beta)$  and the dependence of  $\text{N2O2}$  on  $\text{O3Hb}$  and  $L(\text{H}\beta)$  for the SDSS star-forming galaxy locus ( $\text{N2Ha} < -0.5$ ) using the MPFIT2DFUN two-dimensional fitting routine from Markwardt (2009). This time we adopted a linear dependence for both  $\text{O3Hb}$  and  $L(\text{H}\beta)$ , obtaining

$$\text{N2O2} = -0.71 - 0.75(\text{O3Hb}) + 0.16(\log L(\text{H}\beta) - 40.5) \quad (4)$$

and

$$\text{N2S2} = -0.20 - 0.40(\text{O3Hb}) + 0.17(\log L(\text{H}\beta) - 40.5). \quad (5)$$

In Figure 8, we show these linear fits at the median  $\log L(\text{H}\beta) = 40.5 \text{ erg s}^{-1}$  (green line). In both diagnostic diagrams, compared to this line, the lower-luminosity points lie uniformly low, while the higher-luminosity points lie uniformly high. Because of the weakness of the  $[\text{SII}]6717,6731$  lines and the difficulty of both cross-calibrating the  $[\text{OII}]3726,3729$  and  $[\text{NII}]6584$  lines and applying appropriate extinction corrections, we compare the SDSS data only to the deeper high-redshift galaxy sample of Shapley et al. (2015, orange circles), who carefully treated the relative calibrations of the  $[\text{OII}]3726,3729$  and  $[\text{NII}]6584$  lines. Again, the positions of the high-redshift galaxies in the diagrams closely

match the positions of the higher-luminosity SDSS galaxies. The luminosities of the high-redshift galaxies in Figure 8 lie between  $\log L(\text{H}\beta) = 41.1$  and  $42.6$  with 85% lying in the  $41.5-42.5$  range (Reddy et al. 2015) where we show the SDSS galaxies.

Finally, we consider the  $[\text{OIII}]5007,4861/[\text{OII}]3727$  versus  $([\text{OII}]3727 + [\text{OIII}]5007,4861)/\text{H}\beta$  ( $\text{O32}$  versus  $\text{R23}$ ) diagram, which is a well-known probe of both metallicity and ionization parameter (Kewley & Dopita 2002). (Note that  $[\text{OII}]3727$  is the sum of the fluxes in the  $[\text{OII}]$  doublet.) In Figure 9, we again show the higher-luminosity SDSS sample (light green squares) and the lower-luminosity SDSS sample (black points), together with the Shapley et al. (2015) high-redshift data (orange circles). We include extinction corrections in computing all of these ratios. The positions of the high-redshift galaxies in the diagram are fully consistent with the positions of the higher-luminosity SDSS galaxies, within the  $\text{R23}$  errors (i.e., the high-redshift galaxies are more scattered due to the larger errors).

Now that we have established the similarity of the high-redshift data to the higher-luminosity SDSS data for all the diagnostic diagrams, we return to the BPT diagram to examine in closer detail the redshift evolution of our  $L(\text{H}\beta)$ -selected galaxy sample. In Figure 10, we show the galaxies that satisfy the luminosity limits at which our samples are complete (see Section 2.3) for (a) two



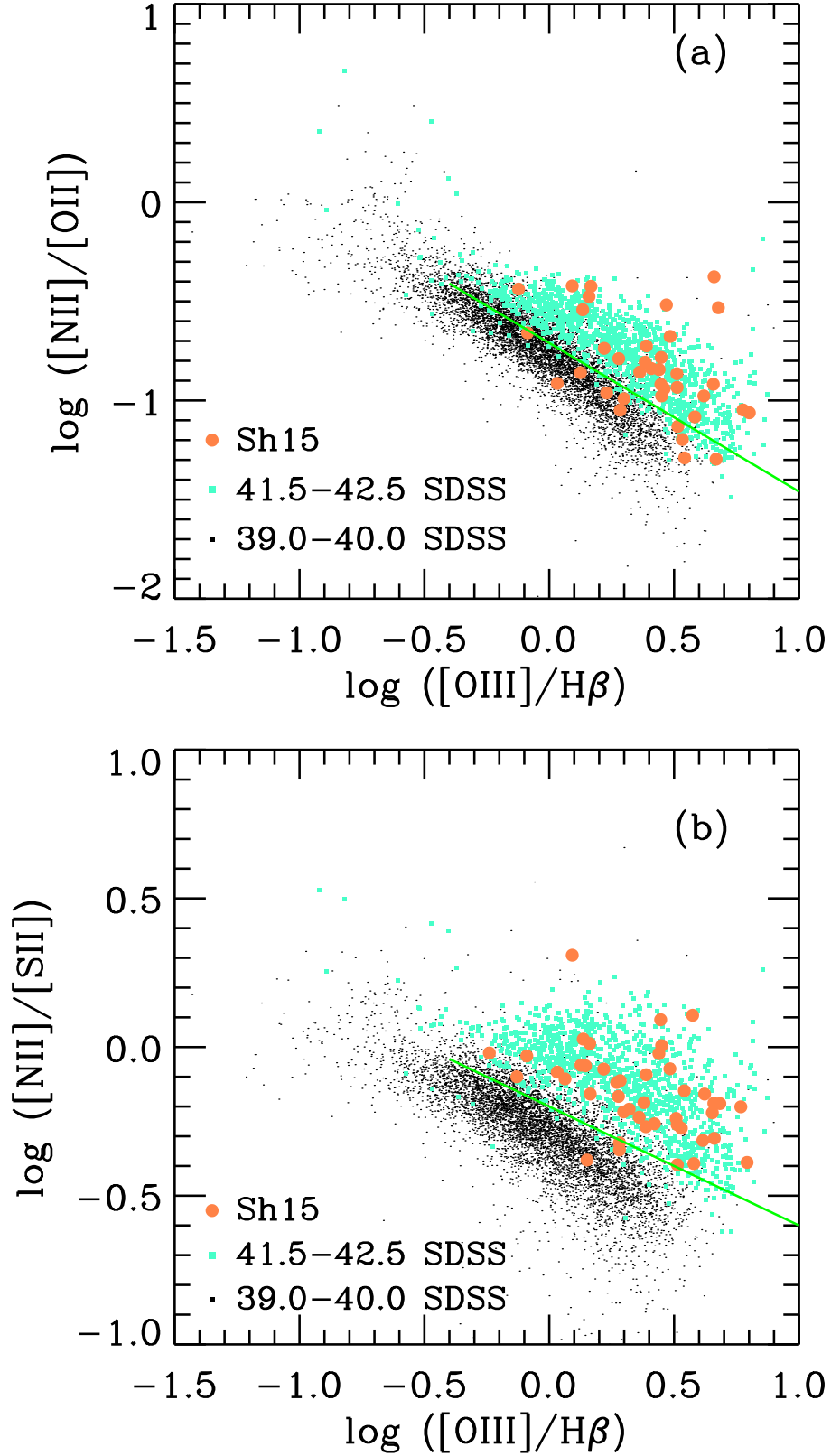


FIG. 8.— (a) N2O2 and (b) N2S2 vs. O3H $\beta$  for the full SDSS sample on the star-forming galaxy locus of the BPT diagram ( $\text{N2Ha} < -0.5$ ) in two intervals of  $\log L(\text{H}\beta)$  (black dots— $39.0-40.0 \text{ erg s}^{-1}$ ; light green squares— $41.5-42.5 \text{ erg s}^{-1}$ ). The green solid lines show linear fits to the star-forming galaxy locus of the full SDSS sample at the median  $\log L(\text{H}\beta) = 40.5 \text{ erg s}^{-1}$ . The orange circles show the high-redshift galaxies from Shapley et al. (2015), which closely match the positions in the diagrams of the higher-luminosity SDSS galaxies. The luminosities of the high redshift galaxies lie between  $\log L(\text{H}\beta) = 41.1-42.6$  with 85% lying in the 41.5-42.5 range (Reddy et al. 2015). Extinction corrections are included in N2O2 for all of the samples, because of the large wavelength separation between the lines.

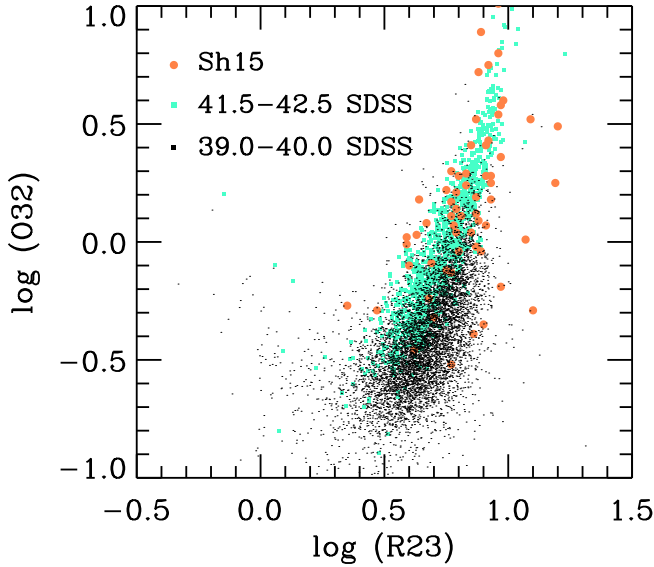


FIG. 9.— O32 vs. R23 for the full SDSS sample on the star-forming galaxy locus of the BPT diagram ( $N2H\alpha < -0.5$ ) in two intervals of  $\log L(H\beta)$  (black dots— $39.0 - 40.0 \text{ erg s}^{-1}$ ; light green squares— $40.5 - 41.5 \text{ erg s}^{-1}$ ). The orange circles show the high-redshift galaxies from Shapley et al. (2015), which closely match the positions in the diagram of the higher-luminosity SDSS galaxies. Extinction corrections are included in both ratios for all of the samples.

high-redshift and (b) two low-redshift intervals. In (a), we show the galaxies with  $\log L(H\beta) > 41.0 \text{ erg s}^{-1}$  and  $z = 1.38 - 1.74$  as blue circles and the galaxies with  $\log L(H\beta) > 41.3 \text{ erg s}^{-1}$  and  $z = 2.03 - 2.30$  as purple circles. The median luminosities are  $\log L(H\beta) = 41.9 \text{ erg s}^{-1}$  for both samples. We made these measurements solely from the MOSFIRE data. In (b), we show galaxies with  $\log L(H\beta) > 40.5 \text{ erg s}^{-1}$  and either  $z = 0.2 - 0.5$  (black circles) or  $z = 0.5 - 1$  (red circles). Here the median luminosities are  $\log L(H\beta) = 40.9 \text{ erg s}^{-1}$  and  $41.5 \text{ erg s}^{-1}$ , respectively. We made the  $z = 0.2 - 0.5$  measurements solely from the DEIMOS data, while we made the  $z = 0.5 - 1.0$  measurements from both the DEIMOS (O3Hb) and MOSFIRE (N2Ha) data. We have included  $1\sigma$  error bars on all the data points based on randomized measurements in the spectra. The error bars are generally very small for O3Hb in the DEIMOS data but much larger in the MOSFIRE data. Note that some of the data points lie off the locus of star-forming galaxies, in the regime consistent with being powered by AGNs.

In both panels, we show the fit to the star-forming galaxy locus of the full SDSS sample ( $N2H\alpha < -0.5$ ) at the median  $\log L(H\beta) = 40.0$  (green solid curve), along with the luminosity-offset locus determined by evaluating Equations 1 and 2, which vary  $N2H\alpha$  (green dotted), at median  $\log L(H\beta)$  values of (a)  $41.9 \text{ erg s}^{-1}$  and (b)  $41.5 \text{ erg s}^{-1}$  (using the median for the  $z = 0.5 - 1$  interval for (b)). As already expected from Figure 7, we see that we can smoothly represent our high-redshift data with increasing luminosity based on the luminosity offset calculated from the SDSS data. Put simply, galaxies of a given  $L(H\beta)$  have the same strong emission-line properties, regardless of redshift.

## 5. LUMINOSITY-ADJUSTED METALLICITY RELATIONS FOR THE SDSS GALAXIES

A major goal of this paper is to explore what underlying properties in the galaxies might be causing the observed offsets with  $\log L(H\beta)$  in the diagnostic diagrams. We do this by examining the various line ratios individually. For reference, the recent compilation of Asplund et al. (2009) gives solar abundances of  $12 + \log(O/H) = 8.69$ ,  $12 + \log(N/H) = 7.83$  and  $12 + \log(S/H) = 7.12$ . The models of Kewley & Dopita (2002) discussed below use the values from Anders & Grevesse (1989):  $12 + \log(O/H) = 8.93$ ,  $12 + \log(N/H) = 8.05$  and  $12 + \log(S/H) = 7.21$ , together with dust depletions of O and N of  $-0.22$  dex.

There are several well-known mechanisms that can produce offsets in the diagnostic diagrams, including changes in the ionization parameter (i.e.,  $q$ , the ratio of the ionizing photon flux to the hydrogen number density), relative abundance variations (including the effects of dust depletion), particularly in the N to O ratio, and changes in the hardness of the ionizing spectrum. If the underlying mechanism(s) are similar in the SDSS and high-redshift samples, then we can parameterize the dependence of the metallicity relations on  $\log L(H\beta)$  using the SDSS sample and generate luminosity-adjusted metallicity relations that may be applicable to the high-redshift samples. However, regardless of whether these relations really apply at high redshift, the addition of the second parameter (i.e., line luminosity) tightens the relations and improves the low-redshift metallicity estimates.

As we shall discuss further below, the N2O2 parameter is insensitive to the ionization and therefore is primarily a measure of the relative N/O abundance (e.g. Pérez-Montero & Contini 2009). The high N2O2 ratio in the high-redshift galaxies has been interpreted as showing that N/O is overabundant in these objects (Masters et al. 2014; Steidel et al. 2014; Shapley et al. 2015). Pérez-Montero & Contini (2009) give an empirical calibration based on local galaxies of

$$\log(N/O) = 0.93(N2O2) - 0.20 \quad (6)$$

which, when combined with Equation 4, gives a relationship for the median track at a given  $\log L(H\beta)$  of

$$\log(N/O) = -0.86 - 0.70(O3Hb) + 0.15(\log L(H\beta) - 40.5) \quad (7)$$

For  $O3Hb=0.00$ ,  $\log(N/O)$  would range from  $-1.08$  at  $\log L(H\beta) = 39$  to  $-0.64$  at  $\log L(H\beta) = 42$ , compared to the adopted solar value of  $-0.86$ , while at  $O3Hb = 0.50$  the range would be  $-1.43$  to  $-0.98$ . However, the uncertainties in the absolute values should be borne in mind. More robustly, we can see from Equation 7 that at a fixed value of O3Hb, high-luminosity objects ( $\log L(H\beta) = 42$ ) would have a N/O abundance which is a factor of 1.7 times higher than the average local galaxy ( $\log L(H\beta) = 40.5$ ); this is the same effect that is seen in the high-redshift samples.

Absent any other effects, the increase in N/O with increasing  $\log L(H\beta)$  will produce an increase of N2Ha at a fixed O3Hb, resulting in a shift in the BPT diagram in the sense that is seen in Figure 5. However the dependence on  $\log L(H\beta)$  is too strong, with a slope of 0.15

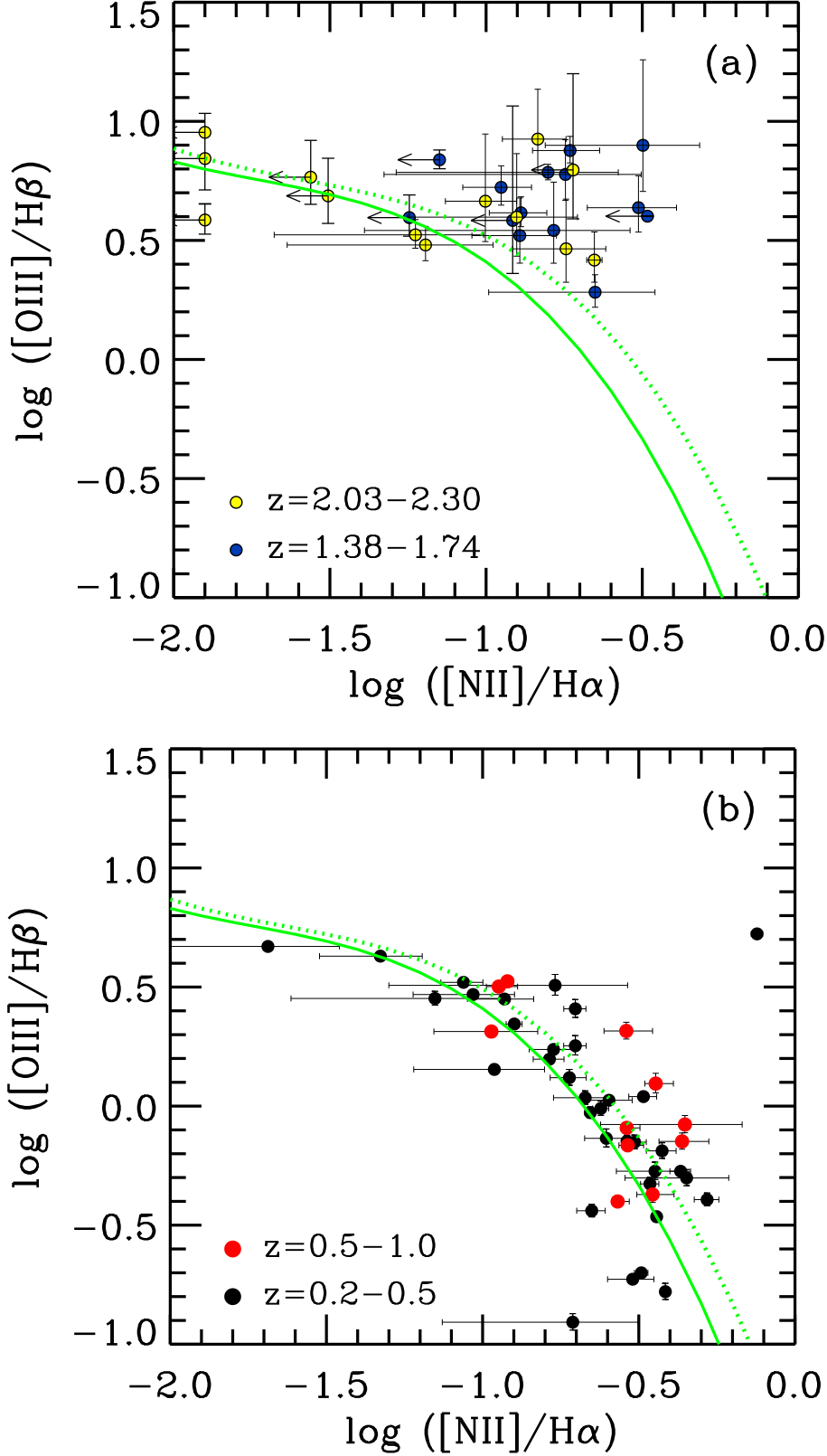


FIG. 10.— Evolution of the BPT diagram to  $z \sim 2.3$  for galaxies in our sample with (a)  $\log L(\text{H}\beta) > 41 \text{ erg s}^{-1}$  (blue circles— $z = 1.38 - 1.74$ ) and  $\log L(\text{H}\beta) > 41.3 \text{ erg s}^{-1}$  (yellow circles— $z = 2.03 - 2.30$ ) using the MOSFIRE data alone, and (b)  $\log L(\text{H}\beta) > 40.5 \text{ erg s}^{-1}$  using either the DEIMOS data alone (black circles— $z = 0.2 - 0.5$ ) or the DEIMOS (O3H $\beta$ ) plus MOSFIRE (N2H $\alpha$ ) data (red circles— $z = 0.5 - 1.0$ ). Source which are not detected in N2H $\alpha$  are shown as one sigma upper limits or at a nominal value of N2H $\alpha = -1.9$ . The  $1\sigma$  error bars on the ratios are larger for the MOSFIRE data than for the DEIMOS data. Note that some of the sources are likely AGNs, given their locations on the diagram. In both panels, the green solid curve shows the fit to the star-forming galaxy locus of the full SDSS sample at the median  $\log L(\text{H}\beta) = 40.4 \text{ erg s}^{-1}$ , while the green dotted curves show the luminosity-offset loci obtained by plugging the median  $\log L(\text{H}\beta)$  values of (a)  $41.9 \text{ erg s}^{-1}$  and (b)  $41.5 \text{ erg s}^{-1}$  into Equations 1 and 2, which vary N2H $\alpha$ .

in Equation 7 compared with 0.09 in the evolution of the BPT diagram (Equations 1-3). This suggests that there must be a countervailing trend that reduces N2Ha for a given O3Hb and reduces the evolution in the BPT diagram.

We investigate this issue by comparing the strong emission-line ratios with direct O abundances, which we calculate using the relations defined in Izotov et al. (2006). We use only SDSS galaxies on the star-forming galaxy locus of the BPT diagram ( $N2Ha < -0.5$ ) where the [OIII]4363 line is strongly detected ( $> 10\sigma$ ). Unfortunately, this strong detection requirement will result in a bias toward lower metallicity (where the [OIII]4363 line is stronger) and higher Balmer-line luminosity, which means we will have a relatively limited dynamic range for determining dependences on  $\log L(H\beta)$ .

### 5.1. $N2O2$ and $N2S2$

We first consider the changes in N2O2 and N2S2. Both these ratios are extremely weakly dependent on  $q$ . At low O abundances relative to solar these line ratios are also almost independent of metallicity (see, e.g. Figures 3 and 4 of Kewley & Dopita 2002).

In Figure 11, we show  $12 + \log(O/H)$  vs. (a) N2O2 and (b) N2S2. We use colored circles to denote three intervals of  $\log L(H\beta)$  (black— $40.5 - 41.0 \text{ erg s}^{-1}$ ; green— $41.0 - 41.5 \text{ erg s}^{-1}$ , and purple— $41.5 - 42.0 \text{ erg s}^{-1}$ ). Over the range  $12 + \log(O/H) < 8.4$ , we assume that N2O2 is independent of  $12 + \log(O/H)$ , and over the range  $12 + \log(O/H) < 8.3$ , we use a linear fit to the extremely weak dependence of N2S2 on  $12 + \log(O/H)$  from Kewley & Dopita (2002) (orange dashed lines). We use these slopes to compute the offsets to the medians of the colored symbols (colored lines), but we do not find the offsets between the luminosity samples to be sensitive to the adopted slopes.

We find that the different luminosity samples can be brought into consistency using offsets that are linear functions of  $\log L(H\beta)$ . In Figure 11(c), we show  $12 + \log(O/H)$  vs.  $N2O2 - 0.29(\log L(H\beta) - 41)$ , and in Figure 11(d), we show  $12 + \log(O/H)$  vs.  $N2S2 - 0.26(\log L(H\beta) - 41)$ . We have checked that the offsets are not sensitive to the choice of the N2Ha limit used to define the star-forming galaxy locus in the BPT diagram, nor to the use of a luminosity-adjusted N2Ha limit (Equations 1 and 2). We also checked that the offsets are not sensitive to the choice of S/N in the [OIII]4363 line detection; we obtained a similar result using a  $5\sigma$  threshold instead of a  $10\sigma$  threshold.

As we have discussed above the offsets in the N2O2 and N2S2 ratios must be understood as arising from changes in the gas-phase abundance ratios of N relative to O and N relative to S, with the higher-luminosity sources being progressively more abundant in N relative to O, and the O and S abundances not changing relative to each other. Since changes in the dust depletion would result in S (which does not deplete onto dust) changing relative to O, it is likely that the changes are in the overall abundances (i.e., gas plus dust) rather than only in the gas-phase abundances.

More specifically, we can interpret Figures 11(c) and 11(d) as implying that the average relations between  $\log(N/O)$  and  $\log(N/S)$  and  $\log L(H\beta)$  for these luminous

galaxies are

$$\log(N/O) = -0.74 + 0.29(\log L(H\beta) - 41), \quad (8)$$

and

$$\log(N/S) = 0.64 + 0.26(\log L(H\beta) - 41). \quad (9)$$

The normalizations in these equations are chosen to match the observed means shown in Figure 11 to the Kewley & Dopita (2002) models shown by the orange dashed lines.

Relative to the local solar value of  $\log(N/O) = -0.86$ , Equation 8 would imply that the high- $L(H\beta)$  galaxies (and hence the high-redshift galaxies) are, on average, over-abundant in N relative to O by a factor of 2.2 at  $\log L(H\beta) = 41.6 \text{ erg s}^{-1}$ .

The above  $L(H\beta)$  dependences derived from the direct O abundance measurements are slightly steeper than the  $L(H\beta)$  dependences of Equations 4, 5 and 7 for N2O2 and N2S2 versus O3Hb. This does not appear to come from variations of O3Hb with luminosity, since, for the observed range of O3Hb, we see no dependence of O3Hb on  $L(H\beta)$  for the galaxies with direct [OIII]4363 measurements. We illustrate this in Figure 12(a), where we show  $12 + \log(O/H)$  versus O3Hb for the same three intervals of  $\log L(H\beta)$  used in Figure 11. The lack of dependence on  $\log L(H\beta)$  is a consequence of the low metallicities and high ionization parameters in the sample with direct O measurements, which result in low values of [OII]/[OIII], and values of [OIII]5007/H $\beta$  that are insensitive to the ionization parameter and metallicity.

Instead, the  $L(H\beta)$  dependences derived from the direct O abundance measurements reflect the bias of galaxies with such measurements toward a more limited range in  $L(H\beta)$ . When we limit the N2O2 and N2S2 vs. O3Hb fits to the same  $L(H\beta)$  range, we find similarly steep relations.

To summarize, our results show that it is the increases in the overall abundance ratios of N/O and N/S that are producing the offsets seen in the N2O2 and N2S2 diagnostic diagrams of Figure 8 for the higher-luminosity SDSS sample. The high-redshift samples are similar in over-abundance to the low-redshift samples with the same high  $L(H\beta)$ .

### 5.2. $N2Ha$

We now examine the change in N2Ha and its role in the observed evolution of the BPT diagram. To do so, we start by considering the Pettini & Pagel (2004) N2Ha calibrator (hereafter, Pettini-Pagel relation), which has been widely used to measure metallicities in high-redshift galaxies, though with some concerns (e.g., Erb et al. 2006; Liu et al. 2008; Newman et al. 2014; Sanders et al. 2015). While empirically the relation between direct O abundance measurements and N2Ha is good at low metallicities (Pettini & Pagel 2004; Maiolino et al. 2008), the relation has always been treated with some suspicion because it is strongly dependent on both the ionization parameter and the abundance ratio of N/O.

Not surprisingly, there is also a dependence of the Pettini-Pagel relation on  $L(H\beta)$ . In Figure 12(b), we show  $12 + \log(O/H)$  versus N2Ha for the same three intervals of  $\log L(H\beta)$  used in Figure 11. Adopting the

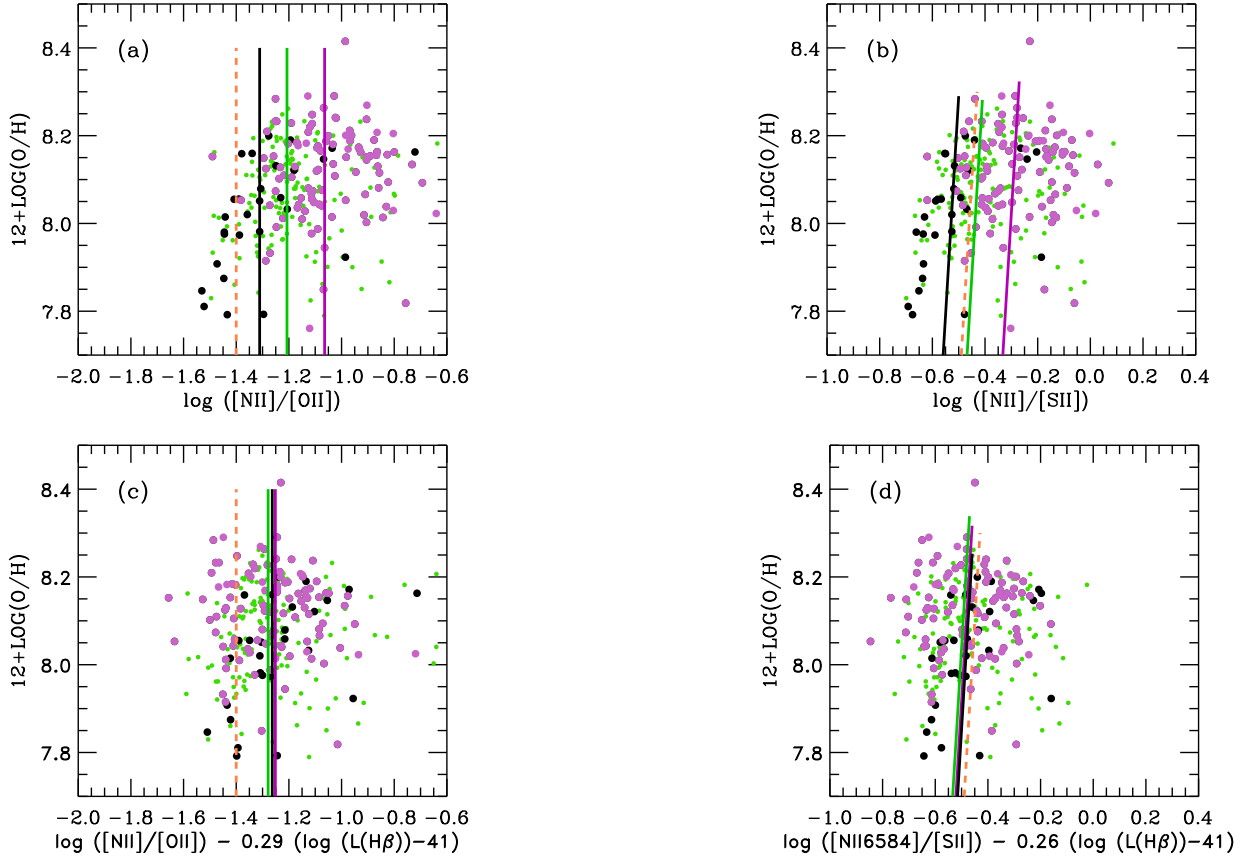


FIG. 11.— Direct O abundance measurements vs. (a) N2O2 and (b) N2S2 for galaxies in the full SDSS sample that lie on the star-forming galaxy locus of the BPT diagram ( $N2Ha < -0.5$ ) and have strong ( $> 10\sigma$ ) [OIII]4363 detections, plotted in three intervals of  $\log L(H\beta)$  (black circles— $40.5 - 41.0 \text{ erg s}^{-1}$ ; green circles— $41.0 - 41.5 \text{ erg s}^{-1}$ ; purple circles— $41.5 - 42.0 \text{ erg s}^{-1}$ ). Our fits to the theoretical values calculated in Kewley & Dopita (2002) are shown as the orange dashed lines. Assuming these shapes, we computed offsets to the median values of the colored symbols (corresponding colored lines). Also shown are directly measured O abundances vs. (c)  $N2O2 - 0.29(\log L(H\beta) - 41)$  and (d)  $N2S2 - 0.26(\log L(H\beta) - 41)$ , which are the luminosity-adjusted values required to bring the samples into alignment.

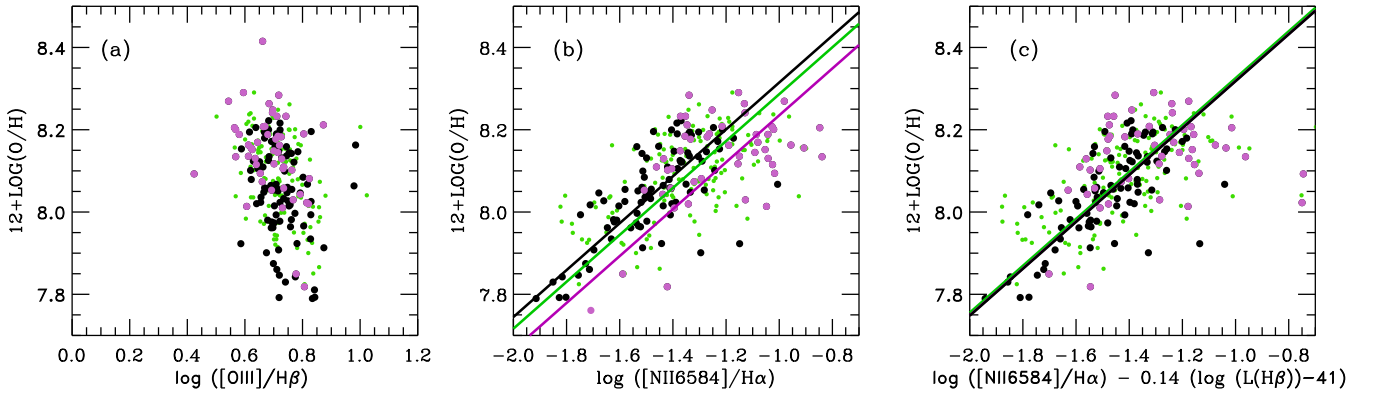


FIG. 12.— (a) Direct O abundance measurements vs. O3Hb for galaxies in the full SDSS sample that lie on the star-forming galaxy locus of the BPT diagram ( $N2Ha < -0.5$ ) and have strong ( $> 10\sigma$ ) [OIII]4363 detections, plotted in three intervals of  $\log L(H\beta)$  (black circles— $40.5 - 41.25 \text{ erg s}^{-1}$ ; green circles— $41.25 - 41.75 \text{ erg s}^{-1}$ ; purple circles— $41.75 - 42.5 \text{ erg s}^{-1}$ ). For the same galaxies, direct O abundance measurements vs. (b) N2Ha and (c)  $N2Ha - 0.14 \log L(H\beta)$  (“adjusted” N2Ha). The colored lines have the Pettini & Pagel (2004) slope and match the median values of the corresponding colored symbols.



slope of 0.57 used by Pettini & Pagel (2004) for their calibration, we match the medians of the colored symbols between  $-2$  and  $-1.3$  (colored lines). We see that the higher- $L(H\beta)$  galaxies have a higher N2Ha for a given direct O abundance. We remove this luminosity dependence in Figure 12(c) by plotting  $\log L(H\beta)$  vs.  $N2Ha - 0.14(\log L(H\beta) - 41)$ . This gives a luminosity-adjusted relation of

$$12 + \log(O/H) = 8.90 + 0.57(N2Ha) - 0.14(\log L(H\beta) - 41). \quad (10)$$

The luminosity correction is large enough to have a significant effect on metal measurements in high-redshift galaxies, which generally will be over-estimated by about 0.1 dex using the uncorrected relation.

The N2Ha dependence on  $L(H\beta)$  is a combination of two effects: the N/O ratio increasing with luminosity, and the ionization parameter increasing with luminosity. These drive the relation between  $12 + \log(O/H)$  and N2Ha in opposite directions, with increasing N/O raising N2Ha for a given O abundance, while increasing  $q$  reduces it.

To disentangle the two effects, we first consider how  $q$  depends on  $L(H\beta)$ . We calculate  $q$  using the Kewley & Dopita (2002)  $[OIII]/[OII]-q$  relation, the parameterization for which is given in Equation 13 of Kobulnicky & Kewley (2004). In cases where the  $[OIII]4363$  line is detected above the  $10\sigma$  level, we again make direct O abundance measurements using the relations defined in Izotov et al. (2006). Otherwise, we use the strong-line-based O abundances given in the value-added SDSS catalog described in Section 2.1, which are calculated using the methods of Tremonti et al. (2004).

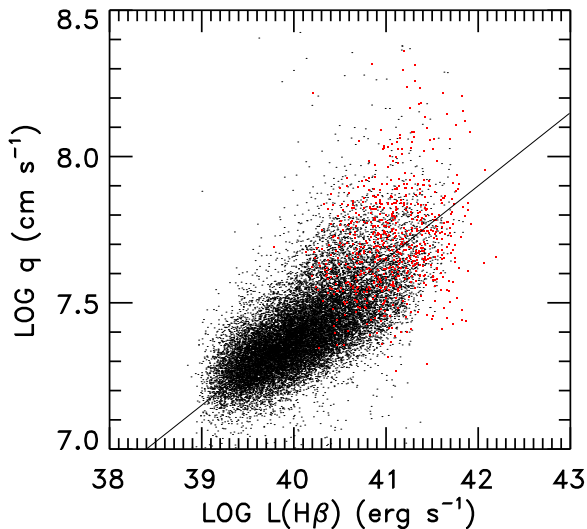


FIG. 13.— Logarithmic ionization parameter vs.  $\log L(H\beta)$ . Red dots show where the O abundances—on which the measurement of  $q$  is based—were determined using the direct method, while the black dots show where the O abundances were determined using the Tremonti et al. (2004) strong-line methodology. The solid line is a linear fit to the data.

As we show in Figure 13, there is quite a tight relation between  $q$  and  $\log L(H\beta)$ . We approximate this with

$$\log q = 7.51 + 0.21(\log L(H\beta) - 41), \quad (11)$$

which we show as the solid line. The galaxies with direct O abundance measurements (red dots) lie primarily in

the high- $L(H\beta)$  regime. This is partly a consequence of higher-luminosity galaxies having higher ionization parameters, and partly a consequence of the selection bias introduced by the higher line S/N in these spectra, since the brighter the galaxy, the more likely it will satisfy the S/N criterion for measuring  $[OIII]4363$ . It is reasonable to ask whether using the strong-line-based O abundances introduces any biases in Equation 11. We have therefore repeated the fit using only the strong-line-based O abundances, but we find essentially the same result.

The range in  $\log q$  is relatively modest, from 7.2 at low  $L(H\beta)$  to 7.9 at high  $L(H\beta)$ , or roughly a multiplicative factor of 4 in  $q$ . As we noted in Cowie & Barger (2008), it is for this reason that even ionization-sensitive diagnostics, such as N2Ha, can be reasonably good metallicity estimators. However, the close dependence of  $q$  on  $\log L(H\beta)$  indicates that the metallicity calibration relations can be improved by including  $L(H\beta)$  as a second parameter.

To determine the effects of the dependence of N2Ha on  $q$ , we make use of the Kewley & Dopita (2002, their Figure 7) model calculations, which we show in Figure 14(a) for the range of  $\log q$  of interest ( $\sim 7.3 - 8.2$ ). For this limited range, we can bring the N2Ha values into consistency by applying a simple offset of  $0.68(\log q - 7.5)$ . We illustrate this in Figure 14(b), where we apply this offset to the models. Below  $12 + \log(O/H) = 9$ , the results are well fit by a linear relation (black line),

$$12 + \log(O/H) = 9.29 + 0.82 \log(N2Ha) + 0.68(\log q - 7.5). \quad (12)$$

Combining Equations 11 and 12 gives

$$12 + \log(O/H) = 9.35 + 0.82 \log(N2Ha) + 0.14(\log L(H\beta) - 41). \quad (13)$$

This has the opposite sign in the dependence on  $L(H\beta)$  from the relation derived from the observational data (Equation 10). However, when we allow for the variation in N/O abundance with  $L(H\beta)$  described by Equation 8, the dependence reverses sign, and Equation 13 becomes

$$12 + \log(O/H) = 9.20 + 0.82 \log(N2Ha) - 0.10(\log L(H\beta) - 41), \quad (14)$$

which is fully consistent with the observational dependence on  $L(H\beta)$ . Equation 14 has a slightly steeper dependence on N2Ha than the Pettini-Pagel relation of Equation 10, but it is in close numerical agreement over most of the fitted range.

The ionization dependence also explains why the evolution in the BPT diagram is weaker than that which would be produced by the evolution in the N/O ratio with  $\log L(H\beta)$  (Equation 8). The increase in  $q$  reduces the  $[NII]6584/[OIII]5007$  ratio and offsets the rise in N2Ha for a given O3Hb produced by the increase in N/O. For  $12 + \log(O/H)$  in the range 8.5 to 9 and  $\log q$  in the range 7.2 to 7.8, Figure 8 of Kewley & Dopita (2002) shows  $[NII]6584/[OIII]5007$  changing as  $-1.2 \log q$ . Combining with Equation 11 translates this to  $[NII]6584/[OIII]5007$  changing as  $-0.25 \log L(H\beta)$ . Combining the ionization reduction with the N/O increase gives N2Ha increasing as  $0.04 \log L(H\beta)$  for a given O3Hb. While this is weaker than the measured value of  $0.09 \log L(H\beta)$  in Equation 1,

it is well within the uncertainties in the calculations. It therefore appears that the offsets in the BPT diagram can be understood as being caused by changes in the N/O abundances, which are partially offset by the changes in the ionization parameter.

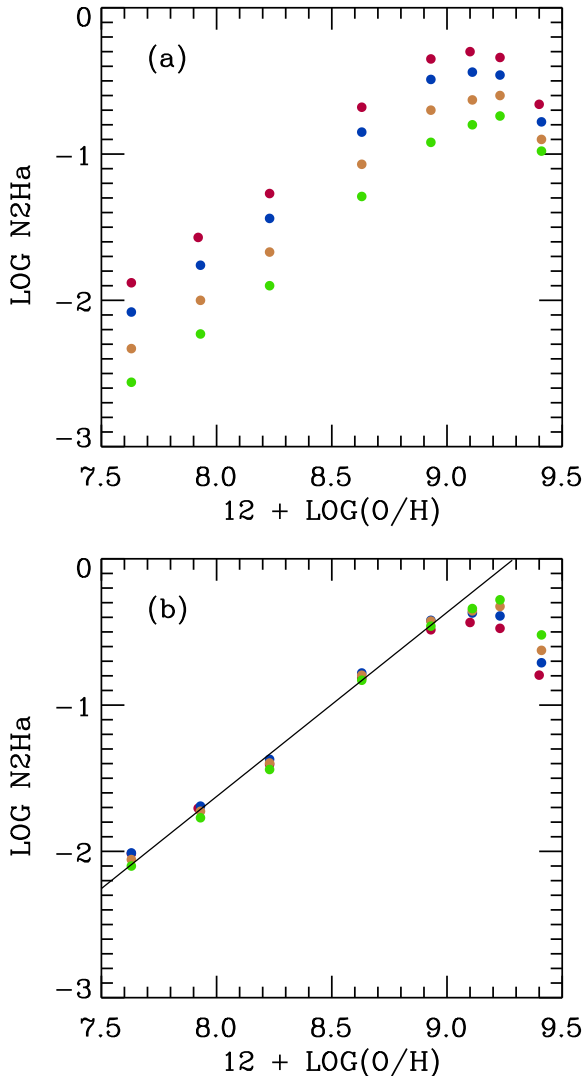


FIG. 14.— N2Ha vs.  $12 + \log(\text{O}/\text{H})$  as a function of the ionization parameter,  $q$ . (a) Model calculations of Kewley & Dopita (2002) taken from their Figure 7. The color of the symbols shows the  $\log q$  parameter ranging from 8.18 (green), 7.90 (gold), 7.60 (blue), to 7.30 (red). (b) Same points from (a) after applying a correction of  $-0.66(\log q - 7.5)$  to  $\text{NH}2\alpha$ . This brings the points into approximate agreement throughout much of the  $12 + \log(\text{O}/\text{H})$  range. Below  $12 + \log(\text{O}/\text{H}) = 9$ , the points in (a) are well fit by the linear relation of Equation 12, which is shown for  $\log q = 7.5$  as the black line in (b).

### 5.3. O32 and R23

The small variation in R23 seen in Figure 9 means that R23 is not a useful metallicity diagnostic for either the high-redshift sample or the higher-luminosity SDSS sample. However, the O32 ratio may be a useful metallicity indicator. Shapley et al. (2015) argued, using the composite spectra for SDSS galaxies from

Andrews & Martini (2013), that there is a strong dependence of galaxy metallicity on position in the O32 versus R23 diagram, with low-metallicity galaxies lying at high O32 and high-metallicity galaxies lying at low O32. They therefore suggested that O32 might be the best approach to measuring the metallicities of high-redshift galaxies.

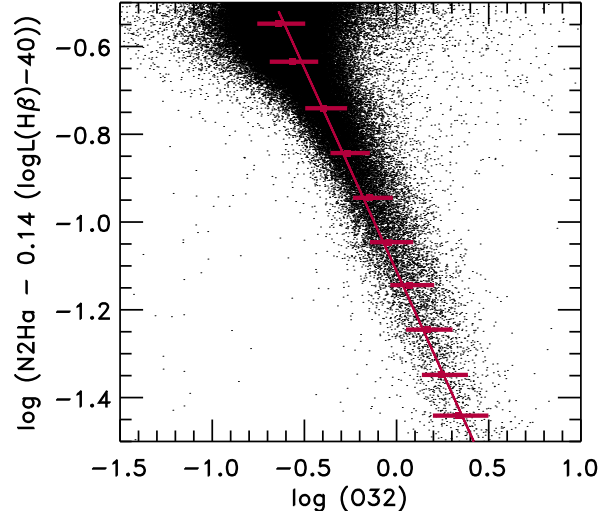


FIG. 15.—  $\text{N}2\text{H}\alpha - 0.17 \log(L(\text{H}\beta) - 40)$  vs. O32 (black dots) for the full SDSS sample on the star-forming galaxy locus of the BPT diagram ( $\text{N}2\text{H}\alpha < -0.5$ ). The red bars show the 68% confidence range in each N2Ha interval, while the red line shows the linear fit of Equation 15.

However, O32 is hard to measure because of the wide wavelength range between the lines, and the necessity for extinction corrections, which require measurements of both  $\text{H}\alpha$  and  $\text{H}\beta$ . Fortunately, we can avoid the use of O32, because it is quite tightly correlated with N2Ha for galaxies in the star-forming galaxy locus of the BPT diagram ( $\text{N}2\text{H}\alpha < -0.5$ ). We illustrate this in Figure 15, where we plot luminosity-adjusted N2Ha versus O32 for galaxies in the full SDSS sample that satisfy this constraint. The luminosity adjustment in N2Ha tightens the correlation and reduces the dispersion by  $\sim 20\%$ . The red bars show the 68% confidence range in each N2Ha interval, and the red line shows a fit of the form

$$\log \text{N}2\text{H}\alpha = -1.11 - 0.93 \log \text{O}32 - 0.14(\log L(\text{H}\beta) - 40). \quad (15)$$

Thus, over the full spread in O32, we can use the much more easily-measured N2Ha as a proxy for O32. A luminosity-adjusted N2Ha is therefore a promising method for measuring the metallicities of high-redshift galaxies.

## 6. SUMMARY

We confirm that all the standard strong emission-line diagnostics for high-redshift galaxies are shifted relative to the average for SDSS galaxies. However, the major result of this paper is that these diagnostics are not shifted relative to SDSS galaxies at similar values of  $L(\text{H}\beta)$ . That is, all galaxies with a given  $L(\text{H}\beta)$  show invariant emission-line properties at all redshifts.

This remarkable result suggests that we can use the easier to study SDSS galaxies as proxies for high-redshift galaxies of the same luminosity. Through such analyses, we showed that the increase of N2Ha, for fixed O3Hb, seen in the BPT diagram as a function of increasing line luminosity is primarily driven by higher N/O abundances in higher-line-luminosity galaxies. However, this effect is partially offset by an increase in the ionization parameter with increasing line luminosity which decreases [NII]6584 relative to [OIII]5007. Changes in N2O2 and N2S2 which increase with  $\log L(\text{H}\beta)$  are driven solely by the increase in N/O with increasing luminosity.

Finally, we argue that we can determine the metallicities of galaxies using a luminosity-adjusted N2Ha parameter for which we provide the equation (Equation 10). Such a luminosity-adjusted N2Ha parameter is much eas-

ier to measure than O32, which also appears to be a useful diagnostic for higher-line-luminosity galaxies.

We thank the referee for very helpful comments that improved the manuscript. We also thank Stephanie Juneau and Christy Tremonti for their valuable input on the first draft of the paper and Naveen Reddy for productive discussions. We gratefully acknowledge support from NSF grants AST-1313309 (L. L. C.) and AST-1313150 (A. J. B) and the University of Wisconsin Research Committee with funds granted by the Wisconsin Alumni Research Foundation (A. J. B.). This research was supported by the Munich Institute for Astro- and Particle Physics (MIAPP) of the DFG cluster of excellence ‘‘Origin and Structure of the Universe’’.

## REFERENCES

- Abazajian, K. N., Adelman-McCarthy, J. K., Agüeros, M. A., et al. 2009, *ApJS*, 182, 543
- Anders, E., & Grevesse, N. 1989, *Geochim. Cosmochim. Acta*, 53, 197
- Andrews, B. H., & Martini, P. 2013, *ApJ*, 765, 140
- Asplund, M., Grevesse, N., Sauval, A. J., & Scott, P. 2009, *ARA&A*, 47, 481
- Baldwin, J. A., Phillips, M. M., & Terlevich, R. 1981, *PASP*, 93, 5
- Barger, A. J., Cowie, L. L., & Wang, W.-H. 2008, *ApJ*, 689, 687
- Brammer, G. B., van Dokkum, P. G., Franx, M., et al. 2012, *ApJS*, 200, 13
- Brinchmann, J., Charlot, S., White, S. D. M., et al. 2004, *MNRAS*, 351, 1151
- Brinchmann, J., Pettini, M., & Charlot, S. 2008, *MNRAS*, 385, 769
- Cowie, L. L., & Barger, A. J. 2008, *ApJ*, 686, 72
- Cowie, L. L., Barger, A. J., Hu, E. M., Capak, P., & Songaila, A. 2004, *AJ*, 127, 3137
- Cowie, L. L., Songaila, A., Hu, E. M., & Cohen, J. G. 1996, *AJ*, 112, 839
- Erb, D. K., Shapley, A. E., Pettini, M., et al. 2006, *ApJ*, 644, 813
- Izotov, Y. I., Stasińska, G., Meynet, G., Guseva, N. G., & Thuan, T. X. 2006, *A&A*, 448, 955
- Juneau, S., Bournaud, F., Charlot, S., et al. 2014, *ApJ*, 788, 88
- Kennicutt, Jr., R. C. 1998, *ARA&A*, 36, 189
- Kewley, L. J., & Dopita, M. A. 2002, *ApJS*, 142, 35
- Kewley, L. J., Yuan, T., Nanayakkara, T., et al. 2015, *ArXiv e-prints*, arXiv:1506.07525
- Kobulnicky, H. A., & Kewley, L. J. 2004, *ApJ*, 617, 240
- Kroupa, P. 2001, *MNRAS*, 322, 231
- Liu, X., Shapley, A. E., Coil, A. L., Brinchmann, J., & Ma, C.-P. 2008, *ApJ*, 678, 758
- Maiolino, R., Nagao, T., Grazian, A., et al. 2008, *A&A*, 488, 463
- Markwardt, C. B. 2009, in *Astronomical Society of the Pacific Conference Series*, Vol. 411, *Astronomical Data Analysis Software and Systems XVIII*, ed. D. A. Bohlender, D. Durand, & P. Dowler, 251
- Masters, D., McCarthy, P., Siana, B., et al. 2014, *ApJ*, 785, 153
- McLean, I. S., Steidel, C. C., Epps, H. W., et al. 2012, in *Society of Photo-Optical Instrumentation Engineers (SPIE) Conference Series*, Vol. 8446, *Society of Photo-Optical Instrumentation Engineers (SPIE) Conference Series*, 0
- Newman, S. F., Buschkamp, P., Genzel, R., et al. 2014, *ApJ*, 781, 21
- Pérez-Montero, E., & Contini, T. 2009, *MNRAS*, 398, 949
- Pettini, M., & Pagel, B. E. J. 2004, *MNRAS*, 348, L59
- Reddy, N. A., Kriek, M., Shapley, A. E., et al. 2015, *ApJ*, 806, 259
- Salim, S., Lee, J. C., Davé, R., & Dickinson, M. 2015, *ApJ*, 808, 25
- Salim, S., Lee, J. C., Ly, C., et al. 2014, *ApJ*, 797, 126
- Sanders, R. L., Shapley, A. E., Kriek, M., et al. 2015, *ApJ*, 799, 138
- Shapley, A. E., Reddy, N. A., Kriek, M., et al. 2015, *ApJ*, 801, 88
- Stasińska, G., Izotov, Y., Morisset, C., & Guseva, N. 2015, *A&A*, 576, A83
- Steidel, C. C., Rudie, G. C., Strom, A. L., et al. 2014, *ApJ*, 795, 165
- Tremonti, C. A., Heckman, T. M., Kauffmann, G., et al. 2004, *ApJ*, 613, 898
- Veilleux, S., & Osterbrock, D. E. 1987, *ApJS*, 63, 295
- Wirth, G. D., Willmer, C. N. A., Amico, P., et al. 2004, *AJ*, 127, 3121
- Wold, I. G. B., Barger, A. J., & Cowie, L. L. 2014, *ApJ*, 783, 119
- Wuyts, E., Kurk, J., Förster Schreiber, N. M., et al. 2014, *ApJ*, 789, L40
- Yabe, K., Ohta, K., Akiyama, M., et al. 2015, *ApJ*, 798, 45